

TAToo: Vision-based Joint Tracking of Anatomy and Tool for Skull-base Surgery

Zhaoshuo Li^{*1}, Hongchao Shu¹, Ruixing Liang^{1,2}, Anna Goodridge¹, Manish Sahu¹, Francis X. Creighton², Russell H. Taylor¹ and Mathias Unberath¹

¹Johns Hopkins University, Baltimore, MD, U.S.

²Johns Hopkins Medicine, Baltimore, MD, U.S.

*Corresponding author(s). E-mail(s): zli122@jhu.edu;

Abstract

Purpose: Tracking the 3D motion of the surgical tool *and* the patient anatomy is a fundamental requirement for computer-assisted skull-base surgery. The estimated motion can be used both for intra-operative guidance and for downstream skill analysis. Recovering such motion solely from surgical videos is desirable, as it is compliant with current clinical workflows and instrumentation. **Methods:** We present Tracker of Anatomy and Tool (TAToo). TAToo jointly tracks the rigid 3D motion of patient skull and surgical drill from stereo microscopic videos. TAToo estimates motion via an iterative optimization process in an end-to-end differentiable form. For robust tracking performance, TAToo adopts a probabilistic formulation and enforces geometric constraints on the object level. **Results:** We validate TAToo on both simulation data, where ground truth motion is available, as well as on anthropomorphic phantom data, where optical tracking provides a strong baseline. We report sub-millimeter and millimeter inter-frame tracking accuracy for skull and drill, respectively, with rotation errors below 1°. We further illustrate how TAToo may be used in a surgical navigation setting. **Conclusion:** We present TAToo, which simultaneously tracks the surgical tool and the patient anatomy in skull-base surgery. TAToo directly predicts the motion from surgical videos, without the need of any markers. Our results show that the performance of TAToo compares favorably to competing approaches. Future work will include fine-tuning of our depth network to reach a 1mm clinical accuracy goal desired for surgical applications in the skull base.

Keywords: Image-based navigation, 3D motion estimation, Computer vision, Deep learning, Computer-assisted interventions

1 Introduction

Many otologic and neurosurgical procedures require that surgeons use a surgical drill to remove bone in the lateral skull-base to gain access to delicate structures therein. This process requires both high precision and a strong visual understanding of the anatomy in order to avoid damages to critical anatomies. If the *rigid* 3D motion of both surgical drill and patient skull can be tracked relative to each-other and provided to the surgeons, we can potentially improve the operation safety through this assistive system [1]. The recovered 3D motion can also be used to assess surgical skill [2] in post-operative analysis.

Despite widespread use of external tracking systems such as optical trackers, video-based solutions are desirable since they integrate seamlessly into existing surgical workflows. Furthermore, for the purposes of skill analysis, they would enable retrospective analysis of videos that were acquired without specialized external tracking instrumentation. However, tracking multiple objects in surgical video streams is challenging due to the need for identification of individual objects and maintaining cross-frame correspondences for motion estimation [3]. Prior video-based systems [4–6] focus on tracking the patient anatomy with respect to the camera but disregard other objects of interest, such as surgical tools. This restricts their applicability to skull-base surgery, where the rigid motion of both patient skull and surgical drill are of interest. Other work [7, 8] assumes no modification of the patient anatomy and requires precise 3D shapes, which is inapplicable to skull-base surgery.

We introduce TAToo (Fig. 1), which simultaneously tracks the rigid 3D motion of patient skull and surgical drill relative to the microscope, without prior 3D information of the surgical scene. Given a stereo video stream as input, TAToo first uses off-the-shelf networks to estimate the stereo depth and segmentation map as a pre-processing step. TAToo then iteratively updates the motion estimate of both patient skull and surgical drill. At each iteration, TAToo matches the correspondences, refines the correspondences in a probabilistic formulation, and lastly regresses consistent object motion based on geometric optimization. The whole method is end-to-end differentiable.

For evaluation, we specifically consider a skull-base surgical procedure named mastoidectomy, where the temporal bone is drilled. As no public dataset is available for our intended application, we collect a set of data for developing TAToo using both simulation and anthropomorphic phantom data emulating the surgical setup (see Fig. 3). We benchmark TAToo against other motion estimation techniques, including keypoint- and ICP-based algorithms. TAToo’s performance compares favorably to competing approaches, and we further find it to be more robust. We show that TAToo achieves sub-millimeter and millimeter tracking accuracy for patient skull and surgical drill, respectively, with

a rotation errors below 1° . We lastly illustrate how TAToo may be used in a surgical navigation setting. Our contributions can be summarized as follows:

- We present a novel framework, TAToo, that tracks the 3D motion of patient skull and surgical drill jointly from stereo microscopic videos.
- We demonstrate that the recovered 3D motion from TAToo can be used in downstream applications, such as a surgical navigation setting.

2 Related Work For 3D Motion Estimation

Motion estimation in general requires matching correspondences temporally and regressing 3D motions based on the matches. **Keypoint-based approaches** detect keypoints from images [9], match keypoints across frames, and then estimate the motion using Procrustes-type registration [10]. In surgical scenes, detecting keypoints can be challenging due to large homogeneous regions. Even if keypoints can be found, the sparsity of the detected points can lead to poor spatial configurations that are not adequate for motion estimation. **ICP-based approaches** [11, 12] instead iteratively find correspondences based on the most recent motion estimate and a set of distance criteria. While the correspondence is often dense and object-level rigidity is enforced, ICP is

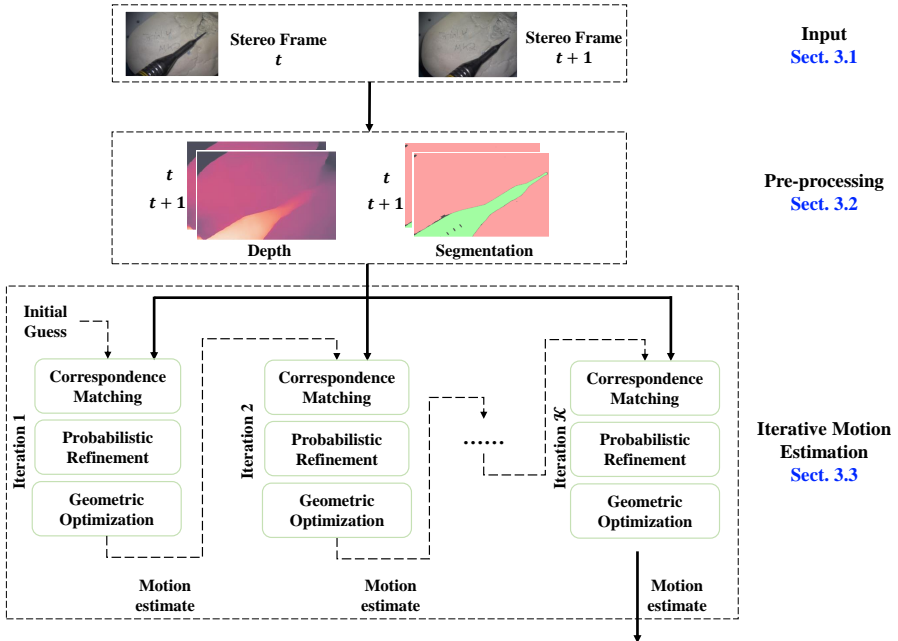


Fig. 1: Overview of TAToo estimating the 3D motion for patient skull and surgical drill. TAToo takes two stereo video frames across time as input (Sect. 3.1), pre-processes the frames (Sect. 3.2) and uses an iterative motion estimation process to regress the motion (Sect. 3.3).

sensitive to outliers [13], which occur often during stereo depth estimation or segmentation estimation. Our approach TAToo builds upon [11, 14, 15] to use all-pixel correspondences with a probabilistic formulation for improved performance. TAToo further enforces object-level constraints based on semantic image segmentation for effective motion tracking of multiple objects.

3 Approach

3.1 Input

We denote the left and right stereo images at a given time as *one stereo frame*. Given stereo frames at time t and $t + 1$ from a microscopic video stream, TAToo recovers the 3D motion of the patient skull and the surgical drill from t to $t + 1$ with respect to the left stereo camera. We use H and W to denote image height and width, subscripts p for *patient skull*, and d for *surgical drill*. We use $T \in \mathbb{SE}(3)$ for rigid 3D motion. The output of TAToo is T_p and T_d , where for convenience of notation we have omitted the temporal dependence.

3.2 Pre-processing

We first use off-the-shelf networks [16, 17] to estimate the depth and segmentation information and the associated prediction probabilities. We denote the depth map as D and probability of the estimate as $\sigma(D)$. The segmentation map, denoted as S , groups pixels to different objects. Each pixel $i \in HW$ belongs to either patient skull ($S^i = p$) or surgical drill ($S^i = d$). The probabilities of the segmentation assignment is denoted as $\sigma(S)$. The depth and segmentation information are estimated for both frames at t and $t + 1$.

3.3 Iterative Motion Estimation

Given an initial guess of the motion of the skull and drill, TAToo iterates between correspondence matching (Sect. 3.3.1), probabilistic refinement (Sect. 3.3.2), and geometric optimization (Sect. 3.3.3). In our work, the initial guess of the motion is set to be zero (*i.e.*, the identity transformation).

3.3.1 Correspondence Matching

Given the most recent 3D motion estimate, we first compute the resulting correspondences across frames.

For each *source* pixel $i_t \in H_t W_t$ from frame t , we compute its *target* location j_{t+1} in frame $t + 1$ given the most recent motion estimate. The correspondence pair is thus formed as i_t, j_{t+1} . To compute j_{t+1} , we use either the patient skull motion T_p or drill motion T_d according to the segmentation prediction S_t^i :

$$j_{t+1} = \pi(T\pi^{-1}(i_t)), \quad T = \begin{cases} T_p, & \text{if } S_t^i = p, \\ T_d, & \text{if } S_t^i = d, \end{cases} \quad (1)$$

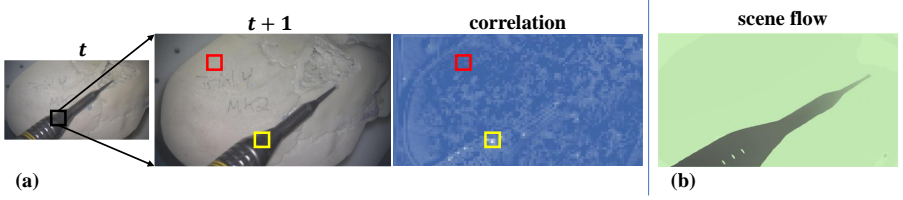


Fig. 2: Qualitative visualization of the motion features. (a) We visualize an $1 \times 1 \times H_{t+1} \times W_{t+1}$ slice of the 4D correlation volume. This slice of correlation corresponds to the correlation between a source pixel in frame t (black) and all pixels in frame $t + 1$. Brighter color indicates larger correlation, *i.e.*, the yellow target pixel has larger correlation with the source pixel than red target pixel. (b) Resulted scene flow between correspondence pairs.

where π and π^{-1} are perspective and inverse perspective projection for conversion between pixel and Cartesian world coordinates.

3.3.2 Probabilistic Refinement

As the correspondence pairs computed from the most recent motion estimate contain outliers, we perform a refinement on these correspondence pairs and estimate the confidence of the refined results. We use a deep learning network to learn how to perform such refinement.

Given a correspondence pair i_t, j_{t+1} , we first evaluate the fitness of the match. Our network extracts features from the *left* images of both stereo frames and builds a 4D correlation volume [14] of $H_t \times W_t \times H_{t+1} \times W_{t+1}$, where dot-product correlation between all features in frame t and all features in frame $t + 1$ are evaluated. A larger value in the correlation volume indicates a more probable match. We retrieve the *correlation* between i_t and j_{t+1} from the 4D correlation volume in Sect. 3.2. We also compute the resulting *scene flow* as $\hat{f}^i = j_{t+1} - i_t$. Both the correlation values and scene flow are used for refinement prediction. A qualitative visualization is shown in Fig. 2.

Using the correlation and scene flow as input, the network then updates the correspondence pair by predicting a *residual update* Δj_{t+1} to the target location j_{t+1} while fixing the source location i_t :

$$\hat{j}_{t+1} = j_{t+1} + \Delta j_{t+1}. \quad (2)$$

In order to evaluate how confident the network is about the update, we also output a probability of such residual update via a sigmoid layer. The refinement probability is denoted as $\sigma(\Delta j_{t+1})$.

Given the updated correspondence pair i_t, j_{t+1}^* , we compute the *joint probability* $\sigma(i_t, j_{t+1}^*)$ of the matching. Intuitively, this joint probability indicates the reliability of the current correspondence pair. We decompose the joint probability $\sigma(i_t, j_{t+1})$ into two terms: 1) the confidence of the information we

know about the source point $\sigma(i_t)$, 2) and confidence of the information we know about the target point $\sigma(\hat{j}_{t+1}|i_t)$:

$$\sigma(i_t, \hat{j}_{t+1}) = \underbrace{\sigma(S_t^i)\sigma(D_t^i)}_{\sigma(i_t): \text{estimate probability}} \underbrace{\sigma(\Delta j_{t+1})\sigma(S_{t+1}^j)\sigma(D_{t+1}^j)}_{\sigma(\hat{j}_{t+1}|i_t): \text{correspondence probability}}, \quad (3)$$

where $\sigma(S_t^i), \sigma(D_t^i)$ are the confidence of depth and segmentation at i_t from frame t , and $\sigma(S_{t+1}^j), \sigma(D_{t+1}^j)$ are the confidence of depth and segmentation at target \hat{j}_{t+1} from frame $t+1$. With a slight abuse of notation, the correspondence probability $\sigma(\hat{j}_{t+1}|i_t)$ is written as a conditional probability because the target locations \hat{j}_{t+1} are computed from i_t . Our network uses a GRU design with convolution layers following prior work on recurrent optimization [14].

3.3.3 Geometric Optimization

Given the matched points and the associated confidence, we regress the motion of both the skull and tool with geometric constraints. We employ Gauss-Newton optimization steps over the $\mathbb{SE}(3)$ space, following its recent success in single object non-rigid tracking [18], structure from motion [19], and SLAM [15]. We estimate motion by minimizing the perspective projection error between the target location \hat{j}_{t+1} and the transformed pixel locations from i_t , weighted by the joint probabilities in Eqn. 3:

$$E(T) = \sum_{i_t \in H_t W_t} \sigma(i_t, \hat{j}_{t+1}) \cdot \|\hat{j}_{t+1} - \pi(T\pi^{-1}(i_t))\|_2, \quad T = \begin{cases} T_p, & \text{if } S_t^i = p, \\ T_d, & \text{if } S_t^i = d, \end{cases} \quad (4)$$

where T_p, T_d are optimized. The intuition behind Eqn. 4 is that, given the perspective projection relationship, as well as the network predicted correspondence and probability, it finds the motion T_p and T_d that best explain the predicted correspondences i_t, \hat{j}_{t+1} .

3.4 Supervision

We adopt a trained off-the-shelf depth network [16] for estimating depth information. We fine-tune a segmentation network [17] on our dataset.

We then train the network in the motion estimation process (Sect. 3.3.2) and impose a loss on the geodesic distance [15] between ground truth and predicted motion for each object on the Lie manifold of $\mathbb{SE}(3)$ [20]:

$$\ell_{\text{geo}} = \|\tau_p\|_2 + \|\phi_p\|_2 + \|\tau_d\|_2 + \|\phi_d\|_2, \quad (5)$$

$$\tau, \phi = \log(T^{\text{GT}}T^{-1}), \quad (6)$$

where T^{GT} is the ground truth motion, τ is the translation vector, and ϕ is the Rodrigues' rotation vector.

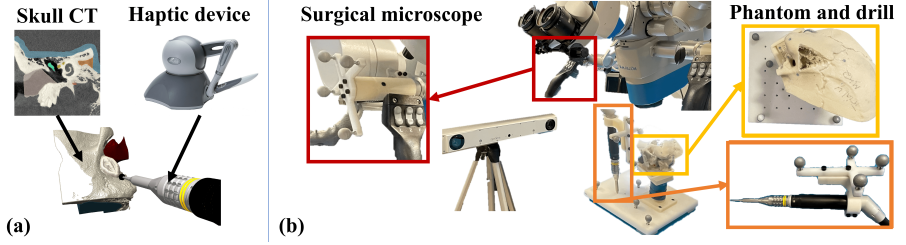


Fig. 3: Data collection setup: (a) simulation environment, (b) surgical phantom with optical tracking as baseline.

Given the ground truth motion, we also derive the match locations j_{t+1}^{GT} and the scene flow $f^{i, \text{GT}}$ for additional supervision, and thus, impose losses as:

$$\ell_{\text{match}} = \frac{1}{H_t W_t} \sum_{i_t \in H_t W_t} |j_{t+1}^{\text{GT}} - j_{t+1}|, \quad (7)$$

$$\ell_{\text{flow}} = \frac{1}{H_t W_t} \sum_{i_t \in H_t W_t} |f^{i, \text{GT}} - f^i|. \quad (8)$$

We note that ℓ_{match} is used to supervise recurrent network incremental estimates Δj_{t+1} , and ℓ_{flow} is used to supervise the motion estimate from the geometric optimization. The refinement probability $\sigma(\Delta j_{t+1})$ is implicitly learnt without any supervision.

The above loss is computed for estimates at each iteration. The summed loss is weighted differently at each optimization iteration:

$$\ell = \sum_{k \in [1, \mathcal{K}]} 0.3^{\mathcal{K}-k} (w_{\text{geo}} \ell_{\text{geo}, k} + w_{\text{match}} \ell_{\text{match}, k} + w_{\text{flow}} \ell_{\text{flow}, k}), \quad (9)$$

where the final iteration is weighted most. We set $w_{\text{geo}} = 10.0$, $w_{\text{flow}} = 0.1$ and $w_{\text{match}} = 0.1$ to balance loss magnitudes.

4 Experimental Setup

4.1 Data

Simulation We use a drilling simulator [21] to generate synthetic data of three different CT scans [22] drilled by surgical residents as shown in Fig. 3(a). For each CT scan, 1500 instances of data are recorded (4500 total). The simulation data contains ground truth depth, segmentation, and motion. The image resolution is 640×480 . We use two sequences for training/validation and one sequence for testing.

Phantom We additionally collect four video sequences of surgical phantom data as shown in Fig. 3(b). We use the Atracsys fusionTrack optical

tracker¹ and mount retro-reflective tracking markers on the surgical microscope, phantom, and drill to acquire individual poses, which are used to compute inter-frame motion. We detail the calibration process in the appendix. There were a total of 13915 instances of data. The image resolution is 960×540 . We use three sequences for training/validation and one sequence for testing.

4.2 Training and Evaluation Setup

We train TAToo on synthetic data and then fine-tune on surgical phantom data. The initial motion estimate is set to be the identity transformation. We use pre-trained depth network [16] since we do not have ground truth depth in the phantom data. We manually annotate 100 frames to fine-tune the segmentation network [17] for the surgical phantom data. We set the number of iterations to $\mathcal{K} = 3$. We use random cropping and color augmentations during the training process. We further sub-sample and also reverse the video frames to augment motion data. We use a 80-20 train-validation split ratio.

For evaluation, we benchmark different motion regression algorithms taking the depth and segmentation estimates as a given input. We report the mean L2 norm of translation and rotation error vectors (Eqn. 6) and threshold metrics of 1 mm and 1° over the entire video sequence. We report full results with standard deviation, p-value and relative error w.r.t the ground truth magnitude in the appendix. We compare our motion estimation technique against a keypoint-based approach using ORB features and brute force matching [9], and the colored ICP algorithm [12] implemented by Open3D [23].

5 Results and Discussion

5.1 Tracking Accuracy

Table 1 summarizes the results from both synthetic and surgical phantom data. In both cases, our method outperforms competing approaches by a large margin.

The keypoint-based approach performs worst due to the sparsity and poor spatial configuration of matches, especially for the surgical drill. When there are fewer than 3 keypoints detected, the keypoint-based approach fails to recover the motion, resulting in high failure rates on both dataset. Even for the surgical phantom, many keypoints are clustered in local patches, which is undesirable for motion estimation. In contrast, ICP and TAToo both use dense correspondences to avoid such failure cases. We visualize the matches found by our method in Fig. 5(a), where the correspondences are evenly distributed across the objects.

ICP is also inferior to TAToo due to insufficient outlier rejection during correspondence search, since rejection is based solely on distance and color [13]. In contrast, TAToo uses a fully probabilistic formulation for the matched correspondences, considering confidences in depth, segmentation and matches

¹<https://www.atracsys-measurement.com/products/fusiontrack-500/>

Table 1: Benchmark result on synthetic and surgical phantom data. For all metrics, lower is better. $\|\tau\|_2$: translation error. $\|\phi\|_2$: rotation error. Failure rate: percentage of the video where motion cannot be recovered.

	Synthetic Data				
	$\ \tau_p\ _2$ (mm)	$\ \phi_p\ _2$ (°)	$\ \tau_d\ _2$ (mm)	$\ \phi_d\ _2$ (°)	Failure Rate
Keypoint	29.9 ± 34.2	2.4 ± 2.8	10.8 ± 7.8	34.0 ± 38.5	19%
ICP	1.5 ± 2.5	0.1 ± 0.1	2.9 ± 3.9	4.2 ± 25.0	0%
TAToo (ours)	0.5 ± 0.9	0.1 ± 0.1	1.1 ± 1.8	0.2 ± 0.4	0%

	Surgical Phantom Data				
	$\ \tau_p\ _2$ (mm)	$\ \phi_p\ _2$ (°)	$\ \tau_d\ _2$ (mm)	$\ \phi_d\ _2$ (°)	Failure Rate
Keypoint	7.5 ± 4.8	0.8 ± 0.5	10.3 ± 2.03	16.5 ± 36.5	30%
ICP	0.7 ± 0.7	0.1 ± 0.1	9.7 ± 4.5	2.0 ± 13.9	0%
TAToo (ours)	0.2 ± 0.2	0.1 ± 0.1	4.8 ± 3.5	0.7 ± 0.8	0%

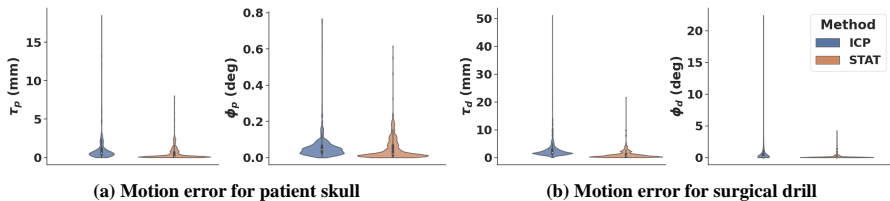


Fig. 4: Violin plots of motion errors comparing ICP and TAToo. TAToo contains much fewer outliers in motion prediction than ICP due to the probabilistic formulation to reject outliers.

to regress the motion. Thus, TAToo can mitigate the effect of outliers and estimate motion more robustly. We show the violin plots of motion errors in Fig. 4 to demonstrate that TAToo indeed contains fewer extreme outliers in prediction due to the improved robustness.

On both data, our approach has better tracking performance for the patient skull than the surgical drill. This is attributed to the larger inter-frame motion of the surgical drill. Indeed, the average motion is 0.1 mm and 0.03° for the skull, but 1.1 mm and 0.38° for the drill.

While our approach compares favorably to other techniques, we note that our performance deteriorates on surgical phantom data compared to synthetic data, especially for surgical drill tracking. We attribute this deterioration, at least partially, to the sim-to-real transfer challenge in the stereo depth estimation network, as we do not have ground truth data to fine-tune the model. It is our future work to investigate techniques to alleviate the sim-to-real transfer issue.

5.2 Downstream Application - Surgical Navigation

We apply our approach to surgical navigation, where inter-frame motion predictions are chained for absolute poses. We report the average drill-to-skull

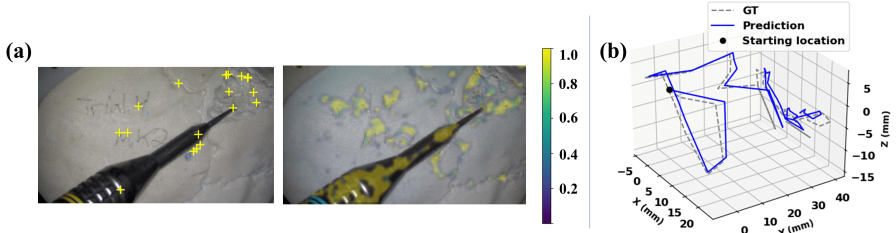


Fig. 5: (a) Spatial distribution of keypoints (yellow crosses, left) and correspondence probabilities $\sigma(i_t, \hat{j}_{t+1})$ of our method (colormap, right) both overlaid on frame t . Our highly probable correspondences are dense and distributed, which is better-conditioned for motion estimation. (b) Plot of surgical drill trajectory in patient coordinate as used in a surgical navigation system.

transformation error over the entire video sequence on the validation set of synthetic data. The average error is 3.6 mm and 0.3° , demonstrating the applicability of the TAToo video-based tracking paradigm in such a setting. A qualitative visualization is shown in Fig. 5(b) and additional visualization can be found in the video supplementary material. While promising, accumulating relative pose for navigation inevitably introduces drift. Additional mechanisms, such as pose graph bundle adjustment, are required to meet the often referenced clinical requirement of <1 mm accuracy [24].

6 Conclusion

We present a stereo video-based 3D motion estimation approach that simultaneously tracks patient skull and surgical drill. Our proposed iterative optimization approach combines learning-based correspondence matching with geometric optimization and probabilistic formulation. Experiments on simulation and phantom data demonstrate that our approach outperforms competing motion estimation methods.

While we show promising results, our evaluation is limited to simulation and phantom data. We plan to further improve our methods, collect *in-vivo* dataset and expand our analysis. Moreover, while TAToo outperforms other image-based tracking algorithms, the accuracy of TAToo does not currently meet our 1 mm clinical accuracy goal, which we attribute to the lack of fine-tuning on the depth network. Future work includes collecting ground truth data for supervising our depth network.

References

- [1] Mezger, U., Jendrewski, C., Bartels, M.: Navigation in surgery. *Langenbeck’s archives of surgery* **398**(4), 501–514 (2013)

- [2] Azari, D.P., Frasier, L.L., Quamme, S.R.P., Greenberg, C.C., Pugh, C., Greenberg, J.A., Radwin, R.G.: Modeling surgical technical skill using expert assessment for automated computer rating. *Annals of surgery* **269**(3), 574 (2019)
- [3] Braspenning, R.A., de Haan, G.: True-motion estimation using feature correspondences. In: *Visual Communications and Image Processing 2004*, vol. 5308, pp. 396–407 (2004). International Society for Optics and Photonics
- [4] Liu, X., Li, Z., Ishii, M., Hager, G.D., Taylor, R.H., Unberath, M.: Sage: Slam with appearance and geometry prior for endoscopy. *arXiv preprint arXiv:2202.09487* (2022)
- [5] Speers, A.D., Ma, B., Jarnagin, W.R., Himidan, S., Simpson, A.L., Wildes, R.P.: Fast and accurate vision-based stereo reconstruction and motion estimation for image-guided liver surgery. *Healthcare technology letters* **5**(5), 208–214 (2018)
- [6] Long, Y., Li, Z., Yee, C.H., Ng, C.F., Taylor, R.H., Unberath, M., Dou, Q.: E-dssr: efficient dynamic surgical scene reconstruction with transformer-based stereoscopic depth perception. In: *MICCAI*, pp. 415–425 (2021). Springer
- [7] Lee, S.C., Fuerst, B., Tateno, K., Johnson, A., Fotouhi, J., Osgood, G., Tombari, F., Navab, N.: Multi-modal imaging, model-based tracking, and mixed reality visualisation for orthopaedic surgery. *Healthcare technology letters* **4**(5), 168–173 (2017)
- [8] Gsaxner, C., Li, J., Pepe, A., Schmalstieg, D., Egger, J.: Inside-out instrument tracking for surgical navigation in augmented reality. In: *Proceedings of the 27th ACM Symposium on Virtual Reality Software and Technology*, pp. 1–11 (2021)
- [9] Rublee, E., Rabaud, V., Konolige, K., Bradski, G.: Orb: An efficient alternative to sift or surf. In: *2011 International Conference on Computer Vision*, pp. 2564–2571 (2011). Ieee
- [10] Kabsch, W.: A solution for the best rotation to relate two sets of vectors. *Acta Crystallographica Section A: Crystal Physics, Diffraction, Theoretical and General Crystallography* **32**(5), 922–923 (1976)
- [11] Besl, P.J., McKay, N.D.: Method for registration of 3-d shapes. In: *Sensor Fusion IV: Control Paradigms and Data Structures*, vol. 1611, pp. 586–606 (1992). Spie

- [12] Park, J., Zhou, Q.-Y., Koltun, V.: Colored point cloud registration revisited. In: *Proceedings of the IEEE International Conference on Computer Vision*, pp. 143–152 (2017)
- [13] Zhang, J., Yao, Y., Deng, B.: Fast and robust iterative closest point. *IEEE Transactions on Pattern Analysis and Machine Intelligence* (2021)
- [14] Teed, Z., Deng, J.: Raft-3d: Scene flow using rigid-motion embeddings. In: *CVPR*, pp. 8375–8384 (2021)
- [15] Teed, Z., Deng, J.: Tangent space backpropagation for 3d transformation groups. In: *CVPR*, pp. 10338–10347 (2021)
- [16] Tankovich, V., Hane, C., Zhang, Y., Kowdle, A., Fanello, S., Bouaziz, S.: Hitnet: Hierarchical iterative tile refinement network for real-time stereo matching. In: *CVPR*, pp. 14362–14372 (2021)
- [17] Shvets, A.A., Rakhlin, A., Kalinin, A.A., Iglovikov, V.I.: Automatic instrument segmentation in robot-assisted surgery using deep learning. In: *ICMLA*, pp. 624–628 (2018). IEEE
- [18] Bozic, A., Palafox, P., Zollhöfer, M., Dai, A., Thies, J., Nießner, M.: Neural non-rigid tracking. *Advances in Neural Information Processing Systems* **33**, 18727–18737 (2020)
- [19] Lindenberger, P., Sarlin, P.-E., Larsson, V., Pollefeys, M.: Pixel-perfect structure-from-motion with featuremetric refinement. In: *ICCV*, pp. 5987–5997 (2021)
- [20] Blanco, J.-L.: A tutorial on se (3) transformation parameterizations and on-manifold optimization. *University of Malaga, Tech. Rep* **3**, 6 (2010)
- [21] Munawar, A., Li, Z., Kunjam, P., Nagururu, N., Ding, A.S., Kazanzides, P., Looi, T., Creighton, F.X., Taylor, R.H., Unberath, M.: Virtual reality for synergistic surgical training and data generation. *AE-CAI*, 1–9 (2021)
- [22] Ding, A.S., Lu, A., Li, Z., Galaiya, D., Siewerdsen, J.H., Taylor, R.H., Creighton, F.X.: Automated registration-based temporal bone computed tomography segmentation for applications in neurotologic surgery. *Otolaryngology–Head and Neck Surgery*, 019459982111044982 (2021)
- [23] Zhou, Q.-Y., Park, J., Koltun, V.: Open3d: A modern library for 3d data processing. *arXiv preprint arXiv:1801.09847* (2018)
- [24] Schneider, D., Mueller, F., Braga, G.O.B., Anschuetz, L., Caversaccio, M., Nolte, L., Weber, S., Klenzner, T.: Evolution and stagnation of image guidance for surgery in the lateral skull. *Frontiers in surgery* (2020)